remote sensing

MDPI

Article

Auto-Tuning of Attitude Control System for Heterogeneous Multirotor UAS

Ayaz Ahmed Hoshu *, Liuping Wang, Abdul Sattar and Alex Fisher

School of Engineering, RMIT University, Melbourne, VIC 3000, Australia; liuping.wang@rmit.edu.au (L.W.); abdul.sattar@rmit.edu.au (A.S.); alex.fisher@rmit.edu.au (A.F.)
* Correspondence: ayaz.hoshu@student.rmit.edu.au

Abstract: This paper presents a heterogeneous configuration of the multirotor unmanned aerial system (UAS) that features the combined characteristics of the helicopter and quadrotor in a single multirotor design, featuring the endurance and energy efficiency similar to a helicopter, while keeping the mechanical simplicity, control, and manoeuvrability of the standard quadrotor. Power needed for a rotorcraft to hover has the inverse relation with the rotor disc. Therefore, multiple small rotors of the quadrotor are energetically outperformed by a large rotor of the helicopter, for a similar size. Designing the stable control system for such a dynamically complex multirotor configuration remains the main challenge as the studies previously carried out on these designs have successfully demonstrated energy efficiency but at the cost of degraded attitude control. Advancements in the energetics of the multirotor results in enhanced endurance and range that could be highly effective in remote operation applications. However, a stable control system is required for accurate positioning. In this paper, a cascaded PID control approach is proposed to provide the control solution for this heterogeneous multirotor. Automatic tuning is proposed to design the PID controller for each loop of the cascade structure. A relay feedback experiment is conducted in a controlled environment, followed by identification of the open-loop frequency response and estimation of dynamics. Subsequently, PID controllers are tuned through approximated models with the help of tuning rules. A custom-designed flight controller is used to experimentally implement the proposed control structure. Presented experimental results demonstrate the efficacy of the proposed control strategy for heterogeneous multirotor UAS.

Keywords: heterogeneous multirotor; cascaded PID control; automatic tuning; stable reference tracking; stable flight operation

check for updates

Citation: Hoshu, A.A; Wang, L.; Sattar, A.; Fisher, A. Auto-Tuning of Attitude Control System for Heterogeneous Multirotor UAS. *Remote Sens.* **2022**, *14*, 1540. https://doi.org/10.3390/rs14071540

Academic Editors : María García Fernández and Guillermo Álvarez-Narciandi

Received: 2 February 2022
Accepted: 18 March 2022
Published: 23 March 2022

Publisher's Note: MDPI stays neutral with regard to jurisdictional claims in published maps and institutional affiliations.

Copyright: © 2022 by the authors. Licensee MDPI, Basel, Switzerland. This article is an open access article distributed under the terms and conditions of the Creative Commons Attribution (CC BY) license (https://creativecommons.org/licenses/by/4.0/).

1. Introduction

Multirotor UASs are privileged with the great characteristics of controllability, rapid manoeuvrability, reliability, diverse applicability, simple design, and economy [1,2], due to which they have yielded feasible solution to a vast variety of civilian as well as military applications [3,4]. Consequently, multirotors have enjoyed considerable attention from both researchers and industrialists in recent years and have been intensively studied lately for their advancements in modelling [5,6], control [7,8], and configuration [9,10]. Multirotor UASs have also played a paramount role in the fight against the COVID-19 pandemic, as they have been extensively used for monitoring social distancing, public announcements, police patrolling, and remote measuring of body temperatures [11]. UASs have also been used to deliver testing kits, vaccines, and other medicinal items during the lockdown [12], and for disinfectant spraying [13]. However, multirotor UASs are termed as less energy-efficient, providing less endurance compared to the fixed-wing and helicopter counterparts of equivalent dimensions [2], which is mainly attributable to interpropeller interference and effect of scale such as Reynolds number. One of the most demanding aspects of the recent popularity of UASs is their applications in remote operations [14,15]. However, the

lack of energetics in multirotors limits their operation in the applications of longer distance and longer flight duration.

Taking more onboard energy storage in order to increase the endurance also contributes to the increment in overall mass of the vehicle, resulting in a further power demand. Thus, the energetics performance attainable by multirotors is naturally limited without the advancements in underlying technology. In the literature, to overcome the endurance and energetics issues of multirotor UASs, certain approaches are instituted. The wireless charging approach proposed in [16] places an extra weight of receiving coil structures and also possesses limitations of charging stations to be established at certain points. For the solar power system utilised in [17], weather variations would have a drastic affect, such as overcast and cloudy conditions, and also would not be beneficial during the night time. Therefore, improving the power transfer efficiency of the multirotor's lifting system through the advancements in rotor configurations would yield enhanced endurance and energy efficiency than previously available strategies as the improvements in the energy density of storage systems is also comparatively slow [18].

The power required by the rotorcraft has the inverse relation with the rotor disc (effective area swept by the rotor) [19]. Therefore, numerous small rotors of a multirotor proportionally demand more power than a helicopter with a large diameter rotor [20]. Whereas helicopters rely upon complex articulated mechanical system for attitude control [21], multirotors achieve it through mechanically simple and articulation-free mechanism. Additionally, helicopters exhibit lack of manoeuvrability and capability for disturbance mitigation due to limited number of degrees-of-freedom to control [22]. Therefore, it would be one of the revolutionary advancements in the field of UASs to improve the energy efficiency of multirotors proportional to a standard helicopter, taking into account the existing features of the multirotors.

A heterogeneous multirotor design is presented here, in which the characteristics of both helicopters and multirotors are incorporated in a single UAS configuration, wherein a single large rotor mounted at the center of the rotorcraft efficiently generates the majority of the required thrust, while four small boom rotors are used to generate control and disturbance rejection forces. Such multirotor configuration results in improved endurance capability and energy efficiency. Furthermore, the boom rotors are opted to be much smaller compared to the standard multirotor (of similar size) with a higher Kv rating, which feature the ability of the faster reaction compared to the rotors of standard multirotor of similar size as well as to the central large rotor of this heterogeneous design. This is because of their decreased inertia. Moreover, Kv represents the motor speed constant defined as revolutions per second (RPM) per volt, illustrating how fast the motor rotates at no load. The similar unconventional multirotor configurations of the heterogeneous nature have also been been explored previously [23,24], where the focus of study is on the advancements in the energy efficiency and compactness of these multirotor unmanned vehicles, wherein the authors have successfully demonstrated the improvements in energetics performance but at the cost of degradation in control performance. The performance of the multirotors can mainly be advanced in two key areas: energy efficiency and control performance. The aerodynamic efficiency of this type of heterogeneous multirotor design has mainly been demonstrated in [23]. While the major scope of this research is to attain the stable and robust control for the heterogeneous multirotor, improvements in the energy efficiency of the multirotor would be highly beneficial, especially in the applications of remote operations where the UAS is required to hover at the longer distances and for longer duration. However, without a stable control system, the objectives of the applications may be not achieved properly as the accurate positioning would also not be possible without a stable and robust UAS control system. Figure 1 shows the proposed configuration of the heterogeneous multirotor UAS.

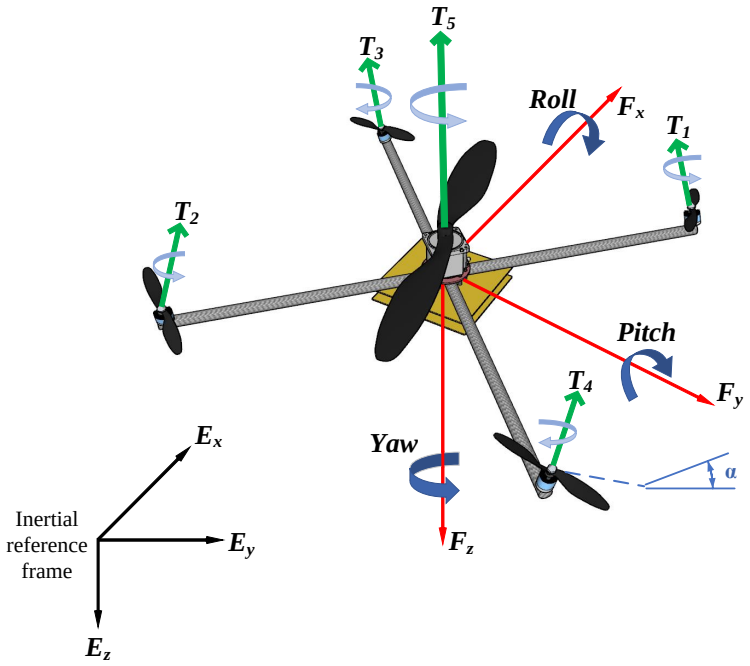

Figure 1. Heterogeneous multirotor model.

Control design of such a heterogeneous configuration has been one of the most challenging aspects towards stable and robust performance of these vehicles [23,24]. This is due to gyroscopic precession, coupled dynamics, complex nonlinearities, and strong multi-channel coupling exhibited by this heterogeneous multirotor. Additionally, it is also an underactuated system (possessing four controlled variables to control six degrees-of-freedom) similar to a conventional quadrotor [25]. For a stable and efficient control system design, the cascade control algorithm is proposed in this paper, which is proven to demonstrate an effective solution for such a dynamically complex and nonlinear multirotor configuration [26]. Several control approaches for multirotors are proposed in the literature, such as model predictive control [27], backstepping control [28], extended state observer [29,30], sliding model control [31], and control through reinforcement learning with disturbance compensation [32]. PID controllers are still most vastly employed [33], due to their ease of practical implementation and simple structure. They also do not require extensive computing power. One of the advantages of PID controllers is the adjustment of controller parameters in the absence of a plant's model information. For the unmanned aerial vehicles, the tuning of the controller parameters can also be performed during online experimental testing [34]. Due to these characteristics, PID controllers are also presently used in most of the mainstream commercial autopilot flight controllers, such as ardupilot [35], micropilot [36], paparazzi auto-pilot [37], multiwii SE V2.0, and afroflight Naze32. Moreover, PID controllers are highly suitable for cascade control architecture due to their convenient tuning of the parameters and smooth implementation. A cascaded PID control structure yields an effective control strategy for the dynamically complex multirotor systems. Whereas the essence is to decompose the overall complex system into multiple small sub-systems and for each decomposed sub-system, the PID controllers are independently tuned solely on the basis on their respective dynamics [38].

Tuning the controller parameters is one of the most challenging tasks when designing the controller for UAS. The cascade control structure associated with the UAS control system additionally complicates the tuning process. For the conventional controller design through plant dynamic model, the large number of parameters would be required, as per multirotor UAS dynamics defined through a set of nonlinear equations. Those physical parameters are often obtained through certain experiments, some of which turn out to be time-consuming and difficult and may also vary as per operating conditions [39]. Moreover,

in the physical model, sensor and actuator dynamics are mostly neglected. Linearized models are also used to simplify the controller design process but at the cost of losing some details of system dynamics. Therefore, considering all these hitches, the model-based PID controller design for multirotors does not necessarily provide a desired performance.

An automatic tuning approach is proposed for the cascade control system of a heterogeneous multirotor. Controller closed-loop experiments are conducted on the multirotor in a controlled experimental environment, through which the time-invariant models are automatically obtained which include the overall multirotor dynamics, including the sensor and actuator dynamics. PID controllers for the cascade control system are then designed utilising the estimated models. The relay feedback experiment on the multirotor is the first step towards the proposed auto-tuning approach. The frequency sampling filter is then applied on the system. Responses obtained through relay feedback test are utilised to recursively approximate closed-loop fundamental frequency [40]. Furthermore, the integrating time delay model is identified and then the PID controllers are tuned, utilising the tuning rules proposed in [41,42]. Finally, a cascade PID control system is implemented and is validated through experimental responses of heterogeneous multirotor UAS. The novel contributions of this paper are summarised as follows:

1. Auto-tuning is performed over a dynamically complex heterogeneous multirotor, where the PID controllers are designed through the experimentally acquired data using relay feedback experiments and system identification, incorporating all of the actual dynamics of the complex configuration, including sensors, actuators, and large rotor gyroscopics.
2. A stable and robust control solution is provided for the heterogeneous multirotor through the auto-tuned cascaded PID control approach. Energy efficiency of these multirotor configurations has been demonstrated in the literature but the stable control performance has remained the major challenge due to the dynamical complexities associated with these designs and gyroscopics, especially due to the introduction of a central large rotor.
3. A hardware prototype is developed to experimentally validate the proposed idea. Additionally, the small boom motors in the prototype used for the manoeuvring control have the capability of faster response time and higher control bandwidth, as these motors are generally associated with the racing drones. Therefore, with the stable control system, these motors lead to faster manoeuvring response of the presented heterogeneous multirotor.
4. A custom flight controller is designed through a high-speed processor (Teensy 3.5), to code and experimentally implement the proposed auto-tuned cascade control algorithm. The presented experimental results demonstrate the efficacy of the proposed idea through real-time flight experiments and comparison with the model-based design approach.

The remainder of this paper is as follows. The energetics of the standard multirotor and heterogeneous multirotor are analytically compared in Section 2. Section 3 illustrates the dynamic model and proposed control structure for this heterogeneous configuration. An automatic tuning algorithm is presented in Section 4. Designs of the hardware prototype and the experimental setup are elaborated in Section 5. The experimental conduction of the auto-tuning for three attitude axes, designing the PID controllers for cascaded control system, and flight test results are discussed in Section 6. The conclusion is drawn in Section 7.

2. Energy Analysis

The momentum theory suggests that the power required by the rotor to hover has a direct relation with the required thrust and inverse relation with the disc area of the rotor.

Let P be the power required by rotor to produce thrust (T) having the disc area (A). Then, P required in hover is expressed as (ideal case) [19]

$$P = T\sqrt{\frac{T}{2\rho A}} \tag{1}$$

where ρ is the air density. For a conventional rotorcraft, T is equal to the vehicle's weight, which leads to the fact that the power demand in a multirotor mainly depends upon the total rotor disc area provided by the specific rotor configuration. In a standard quadcopter, the thrust force on an individual rotor is one fourth of the total. Subsequently, the rotor's area (A) comprises four discs, as shown in Figure 2. Moreover, an appropriate spacing is also required between the rotors considering the interactions of the blade vortices; the rule of thumb is approximately $\sqrt{2}$ times the radius of the rotor [43]. Subsequently, the area available for the lift to a standard quadrotor is significantly less than a conventional helicopter. Therefore, for a conventional quadrotor, the requirement of the total lifting power will be greater than a conventional helicopter, with a rough estimate of about 25% more [18].

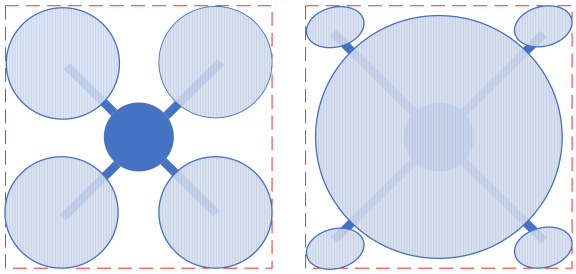

Figure 2. Comparison of the rotor disc area under a given footprint for a conventional quadrotor and heterogeneous multirotor UASs.

The heterogeneous multirotor features a comparable rotor disc footprint to a helicopter as shown in Figure 2. The energetics of a central large rotor of this configuration are comparable to a standard helicopter. A similar triangular heterogeneous multirotor presented in [23] accounts for 20% less power than a standard quadrotor for the given footprints. Moreover, hover efficiency and disc loading are the important attributes to be considered for characterising the energy efficiency of a rotorcraft [44]. Disc loading relates the mass of an aircraft with rotor disc area, whereas hover efficiency relates the mass of the vehicle with the power required to hover. They are expressed as

$$D.L = \frac{m}{A} \tag{2}$$

$$\eta_H = \frac{m}{P} \tag{3}$$

Here, m represents the mass of aerial vehicle, $D.L$ is disc loading, and η_H is hover efficiency. It is to be observed that the disc loading has the inverse relation with the rotor disc area. A low disc loading is generally considered a direct indicator of high lift thrust efficiency. Subsequently for a given weight, a conventional quadrotor with smaller rotors would exhibit higher disk loading and would need more power to hover [45]. Considering T equal to the weight of the rotorcraft and substituting (2) and (3) into (1) provides

$$\eta_H = \frac{1}{g\sqrt{\frac{g}{2\rho}D.L}} \tag{4}$$

It is suggested in (4) that the hover efficiency has an inverse relation with the square root of disk loading. Therefore, a large rotor disc area leads to lower disc loading, which

results in increased hover efficiency. This analytical prediction in (4) is also validated by [24] through actual test data provided by the APC propellers database available at [46].

Moreover, performance and efficiency of the multirotor can also be analysed through the Reynolds number of the propellers. Reynolds number is proportional to the diameter of the propeller such that small-scale propellers operate at much lower Reynolds number compared to the large propellers. Performance and efficiency of the multirotor increase with the Reynolds number. The effect of the Reynolds number and the size of the rotor on the efficiency of the rotorcraft has been experimentally analysed through various-sized propellers in [47], in static as well as advancing flow conditions, where the authors have demonstrated the improvements in the energetics performance of the propellers with the Reynolds number and have concluded that as the size of the propeller increases, thrust co-efficient increases, and power co-efficient decreases.

Furthermore, the main motor used in this work, T-Motor U5 400 KV with 15 × 5 propeller produces 1490 g of thrust consuming 175.38 Watts at 65% of throttle, providing the hovering efficiency of 8.50 g/W as provided by the T-motor testing report [48], whereas the motor which can appropriately be utilised for a conventional quadrotor design of similar footprint (to this heterogeneous multirotor), such as T-Motor AS2814 1050 KV with 10 × 5.5 propeller, produces a thrust of 1165 g at 228.35 Watts at 65% of throttle, with the hover efficiency of 5.10 g/W as available at [49].

3. Dynamic Model and Cascade Control Architecture

In the presented heterogeneous multirotor configuration, the majority of the required thrust is efficiently provided by the large central rotor, similar to a helicopter. The manoeuvring control is achieved through the small boom rotors, similar to a standard quadrotor. However, these are not supposed to offer significant lifting thrust, unlike a conventional quadrotor. These boom rotors have been marginally angled sideways at a fixed cant angle to generate a lateral thrust to counter the torque of the large central rotor, similar to the small tail rotor in a standard helicopter. The manoeuvring moments are attained through the thrust caused by counter-torque rotors. Consequently, through a similar standard quadrotor mechanism, control torques are generated through increasing the speed of specific rotors and subsequently decreasing the speed of other rotors.

3.1. Dynamic Model

The body-fixed frame and the earth-fixed frame are the two reference frames utilised for studying system dynamics of the multirotor. In the earth-fixed frame, the three Euler angles are described as $\eta = [\phi, \theta, \psi]^T$, where roll angle ($\phi$), pitch angle ($\theta$), and yaw angle ($\psi$) represent the rotation around x-axis, y-axis, and z-axis, respectively. In the body-fixed frame, the angular velocities of a rotorcraft are represented as $\Omega = [p, q, r]^T$, where p, q, and r are the roll, pitch, and yaw angular velocities, respectively. Moreover, the rotational acceleration of the multirotor in the body-fixed frame is described by the equations of motion as follows [50]:

$$\dot{p} = \frac{(I_{yy} - I_{zz})qr}{I_{xx}} + \frac{\tau_x}{I_{xx}} + \frac{J_r q\omega}{I_{xx}} \tag{5}$$

$$\dot{q} = \frac{(I_{zz} - I_{xx})pr}{I_{yy}} + \frac{\tau_y}{I_{yy}} + \frac{J_r p\omega}{I_{yy}} \tag{6}$$

$$\dot{r} = \frac{(I_{xx} - I_{yy})pq}{I_{zz}} + \frac{\tau_z}{I_{zz}} \tag{7}$$

Here, I_{xx} represents the moment of inertia for x-axis; similarly, I_{yy} and I_{zz} account for y and z axes, respectively, and τ_x, τ_y, and τ_z are the torques for roll, pitch, and yaw, respectively. $J_r p\omega$ and $J_r q\omega$ express the propellers' gyro effects, where J_r and ω account for

the inertia and speed of rotor. Furthermore, angular velocities acquired through the above expressions are then converted to earth-fixed frame through the following approach:

$$\dot{\eta} = N\Omega \tag{8}$$

Here, N represents transformation matrix, which is expressed as

$$N = \begin{bmatrix} 1 & \sin\phi\tan\theta & \cos\phi\tan\theta \\ 0 & \cos\phi & -\sin\phi \\ 0 & \sin\phi\sec\theta & \cos\phi\sec\theta \end{bmatrix} \tag{9}$$

The rotor's thrust (T_i) and drag torque Q_i are defined as

$$T_i = b\omega_i^2 \tag{10}$$

$$Q_i = k_d\omega_i^2 \tag{11}$$

k_d and b are drag and thrust coefficients, whereas ω_i represents the individual rotor's rotational speed.

The roll, pitch, and yaw moments in the multirotor are obtained through appropriate controlling of the thrust difference among small arm rotors. Total thrust T and the torques for roll, pitch, and yaw are formulated as

$$\begin{bmatrix} T \\ \tau_x \\ \tau_y \\ \tau_z \end{bmatrix} = \begin{bmatrix} bC\alpha & bC\alpha & bC\alpha & bC\alpha & b_M \\ -\frac{1}{\sqrt{2}}blC\alpha & \frac{1}{\sqrt{2}}blC\alpha & \frac{1}{\sqrt{2}}blC\alpha & -\frac{1}{\sqrt{2}}blC\alpha & 0 \\ -\frac{1}{\sqrt{2}}blC\alpha & \frac{1}{\sqrt{2}}blC\alpha & -\frac{1}{\sqrt{2}}blC\alpha & \frac{1}{\sqrt{2}}blC\alpha & 0 \\ -blS\alpha - k_dC\alpha & -blS\alpha - k_dC\alpha & blS\alpha + k_dC\alpha & blS\alpha + k_dC\alpha & -k_{dM} \end{bmatrix} \begin{bmatrix} \omega_1^2 \\ \omega_2^2 \\ \omega_3^2 \\ \omega_4^2 \\ \omega_5^2 \end{bmatrix} \tag{12}$$

where α is the tilt angle of the small rotors, S_α and C_α represent $\sin(\alpha)$ and $\cos(\alpha)$, respectively, b_M and k_{dM} are the thrust and drag coefficients of the large rotor, and l denotes distance between small motors and centre of the unmanned vehicle.

3.2. Cascade Control System

The presented heterogeneous configuration of a multirotor system is an underactuated system, possessing coupled dynamics and nonlinearities as well as strong coupling among multi-input multi-output channels. Therefore, devising a stable and robust control strategy for such an unconventional UAS has been the most difficult aspect towards a successful flight. Degraded attitude control performance has been reported in the literature by the previous studies carried out on the heterogeneous multirotor configuration [23,24]. Cascaded PID control algorithm is proposed in this paper to attain a robust and stable attitude control performance, which is implemented through a custom-designed flight controller over a high speed microprocessor, in order to ensure stability of the presented rotorcraft, also under the disturbances.

In a multirotor control system, the control manipulated variables are torques (τ_x, τ_y, and τ_z) for angular control and force (f) for altitude control. The control objective for the multirotor system is to ensure the effective tracking of the reference signals (ϕ^*, θ^*, and r^*) and mitigating any disturbances. The proposed cascaded PID control structure implemented through a custom designed flight controller will stably achieve these control objectives and will also effectively deal with existing couplings and nonlinearities, offering enhanced disturbance rejection characteristics.

The algorithm of cascade control relies upon the decomposition of the complex system into various simple and small sub-systems, allowing PID controllers for each decomposed sub-system to be independently designed [42], which leads to an effective solution to the control problems for a system that exhibits complexities in dynamics. The attitude control system is responsible for maintaining the required 3D orientation of the UAS, and is therefore regarded as the heart of the UAS control system. Both rotational and translational

movements for a rotorcraft are obtained via attitude control. To design the cascade control structure for a multirotor, attitude dynamics are decomposed as inner loop (angular rates) and outer loop (angular position). Figure 3 demonstrates the proposed architecture for the cascaded control system for a heterogeneous multirotor. PID controllers are used to control the inner loop system, providing angular rate control, whereas PD controllers are employed to control the outer loop system, providing angular position control. Integral term is not used for the outer loop system because there already exists an integrator in the outer plant dynamics, as presented in (8). Adding the integral controller in the outer loop provides oscillatory response.

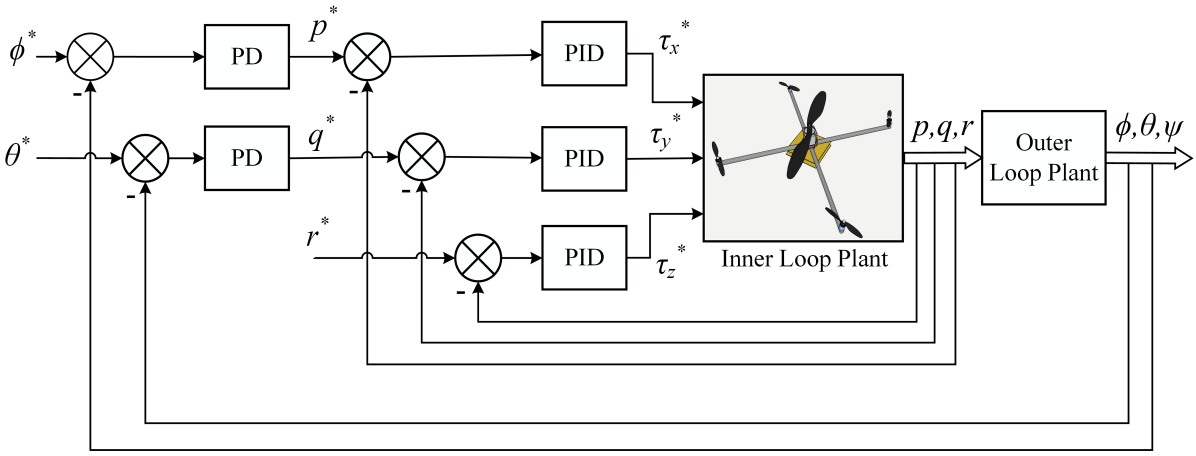

Figure 3. Cascade control structure for attitude control of heterogeneous multirotor.

4. Auto-Tuner Design for Cascaded PID Controllers

Tuning the PID controllers is the next key step in designing a control system after configuring the control system architecture. In this paper, the auto-tuning approach is proposed to automatically obtain the required parameters of the PID controllers.

4.1. Relay Feedback Experiment

Frequency response of the multirotor is initially identified using the relay feedback control experiment. Sustained oscillations are obtained in a closed-loop operation through relay experiment. In a cascade control environment, inner loop is tuned first. Therefore, auto-tuning is firstly performed on angular rate control loop, and, based on the estimated inner loop dynamics, the outer loop is tuned. A proportional controller (K_T) is used for stability purpose as the dynamic system contains an integrator. Figure 4 illustrates the relay feedback experiment setup for roll angular rate.

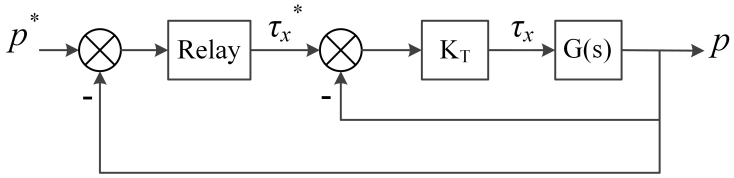

Figure 4. Relay feedback experiment for roll axis.

4.2. Identification of Frequency Response and Estimation

A frequency sampling filter (FSF) is used to extract the useful information from the data acquired through relay feedback experiment [51,52]. The set of periodic input ($u(k)$) and output ($y(k)$) signals is acquired through successful relay experiment having

the fundamental discrete frequency as $\omega_d = 2\pi/N$. Here, N is the period in number of samples. The output is described, utilising FSF model in relation to input signal, as

$$y(k) = G(0)f^0(k) + \sum_{l=-(n-1)/2}^{(n-1)/2} G(e^{jl\omega_d})f^l(k) + v(k) \tag{13}$$

where l = 1, 2, 3,..... N, $G(0)$ and $G(e^{jl\omega_d})$ are the plant frequency response points, and $v(k)$ represents the output measurement noise that is supposed to be Gaussian distributed having zero mean and variance σ^2. Moreover, $f^l(k)$ is the FSF output vector and $f^0(k)$ is the output of FSF at zero frequency, expressed as

$$f^l(k) = \frac{1}{N}\frac{1-q^{-N}}{1-q^{-1}e^{jl\omega_d}}u(k) \tag{14}$$

$$f^0(k) = \frac{1}{N}\frac{1-q^{-N}}{1-q^{-1}}u(k) \tag{15}$$

q^{-1} here denotes the back-shift operator, expressed as $q^{-1}x(k) = x(k-1)$.

For a perfect periodic input signal $u(k)$ having period N, the Fourier analysis [53] suggests that it possesses an odd number of frequencies only, and a decaying magnitude with the increasing number. Practically, due to the effect of noise or nonlinearity, it is rare for the $u(k)$ to be a perfect periodic signal, hence, the output signal, through neglecting the high frequency terms, is expressed as

$$\begin{aligned} y(k) \approx\ & G(e^{j0})f^0(k) + G(e^{j1\omega_d})f^1(k) + G(e^{-j1\omega_d})f^{-1}(k) + G(e^{j2\omega_d})f^2(k) + G(e^{-j2\omega_d})f^{-2}(k) \\ & + G(e^{j3\omega_d})f^3(k) + G(e^{-j3\omega_d})f^{-3}(k) + v(k) \end{aligned} \tag{16}$$

The vector having complex parameters and its correlating regressor vector can be presented as

$$\Theta = [G(0)G(e^{j\omega_d})G(e^{-j\omega_d})G(e^{j2\omega_d})G(e^{-j2\omega_d})G(e^{j3\omega_d})G(e^{-j3\omega_d})]^* \tag{17}$$

$$\Phi = [f^0(k)f^1(k)f^{-1}(k)f^2(k)f^{-2}(k)f^3(k) + f^{-3}(k)]^* \tag{18}$$

Here, $*$ suggests the transpose of complex conjugate of the concerned variable. A recursive least square algorithm is used to calculate the approximated frequency parameter vector, such as $\hat{\Theta}(k)$, which is expressed as

$$P(k) = P(k-1) - \frac{P(k-1)^*\Phi(k)\Phi(k)^*}{1 + P(k-1)\Phi(k)\Phi(k)^*} \tag{19}$$

$$\hat{\Theta}(k) = \hat{\Theta}(k-1) + P(k-1)\Phi(k)[y(k) - \Phi(k)^*\hat{\Theta}(k-1)] \tag{20}$$

The plant frequency response $G(e^{j\omega_d})$ is derived through the relationship with closed-loop frequency response and with the knowledge of K_T.

$$T(e^{j\omega_d}) = \frac{G(e^{j\omega_d})K_T}{1 + G(e^{j\omega_d})K_T} \tag{21}$$

Frequency response for the open loop system is then calculated as

$$G(e^{j\omega_d}) = \frac{1}{K_T}\frac{T(e^{j\omega_d})}{1 - T(e^{j\omega_d})} \tag{22}$$

It is noteworthy that frequency response in discrete time $G(e^{j\omega_d})$ is closely approximated to the continuous time counterpart, considering that the system is operating under a fast sampling environment, where $\omega_1 = \omega_d/\Delta T$ is the equivalent continuous time

frequency. If $G_p(j\omega_1)$ represents continuous time frequency response for the plant at fundamental frequency ω_1, it can be written as

$$G_p(j\omega_1) \approx G(e^{j\omega_d}) \tag{23}$$

A single frequency is adequate to calculate the time delay (d) and the gain (K_p) for the integrator plus time delay model, where an estimated model is supposed to be

$$G_p(s) = \frac{K_p e^{-ds}}{s} \tag{24}$$

Both decomposed sub-systems possess dominant dynamics, having poles either closer to origin (inner sub-system) or on the origin of complex plane (outer sub-system). Time delay component is utilised to estimate small time constants associated with the system, such as sensors and actuators, considering the integrator plus delay model frequency response to be equal to the approximated $G_p(j\omega_1)$ results.

$$\frac{K_p e^{-jd\omega_1}}{j\omega_1} = G_p(j\omega_1) \tag{25}$$

K_p is calculated by solving (25) and is expressed as

$$K_p = \omega_1 |G_p(j\omega_1)| \tag{26}$$

where $|e^{-jd\omega_1}| = 1$. Approximation of time delay can be obtained if we compare the phase angle at both sides of (25), provided as

$$d = -\frac{1}{\omega_1} \tan^{-1} \frac{Imag(jG_p(j\omega_1))}{Real(jG_p(j\omega_1))} \tag{27}$$

4.3. Pid Tuning

After obtaining the estimated integrating delay model, parameters of the PID controller are determined utilising the tuning rules presented in [40,54]. These set of tuning rules provide attributes of being robust and simple. PID controller values are determined through the following normalised parameters.

$$K_c = \frac{\hat{K}_c}{dK_p} \tag{28}$$

$$\tau_I = d\hat{\tau}_I \tag{29}$$

$$\tau_D = d\hat{\tau}_D \tag{30}$$

Considering the damping coefficient as $\xi = 1$, these normalised parameters are formulated as

$$\hat{K}_c = \frac{1}{0.05080\beta + 0.6208} \tag{31}$$

$$\hat{\tau}_I = 1.9885\beta + 1.2235 \tag{32}$$

$$\hat{\tau}_D = \frac{1}{1.0043\beta + 1.8194} \tag{33}$$

where β is scaling factor that is chosen as per required closed-loop time constant, used as $\tau_{cl} = \beta d$.

5. Experimental Setup

A custom-designed heterogeneous multirotor is built to carry out the experimentation for the proposed idea, as shown in Figure 5. Table 1 presents the physical specifications of the prototype. The small boom motors are required to provide fast actuator response as

they are responsible to not only provide control moments but also to tackle the gyroscopics from the large central rotor. Therefore, the motors of the higher kV rating are chosen, which offer high RPM and decreased inertia, possessing the potential to react faster.



Figure 5. Heterogeneous multirotor prototype.

Attitude of the multirotor is robustly estimated through combination of IMU (inertial motion unit) and digital motion processor (DMP) through quaternions approach [55]. Employing the dedicated DMP features the advantage of providing noise-free attitude information and also relieving the main processor from extra motion processing data. A high-speed micro-controller is required for this heterogeneous multirotor, which assesses the attitude information and accordingly provides the control signal to the actuators in order to benefit from the fast-reacting boom rotors. Therefore, a Cortex M4 processor (32-bit) is used to implement the control system. Figure 6 presents the configuration of the designed custom flight control system, whereas the flight controller's specifications and avionic parts are depicted in Table 2.

To perform the tuning procedures, custom-designed test rigs are developed for the purpose of replicating the flight conditions, while the multirotor is kept under a controlled environment. The multirotor is then fixed on the test rig, along its thrust line, allowing only the specific motion, individually isolating the axis under consideration. These rigs are especially useful during the identification procedure, as experiments will not be affected by the coupling from remaining axes, while dynamics of the system under analysis are accurately estimated for the considered axis. Two test rigs are developed; Figure 7 illustrates the test rig for roll and pitch axis, whereas the test rig shown in Figure 8 is used to analyse the attitude of the multirotor for yaw axis.

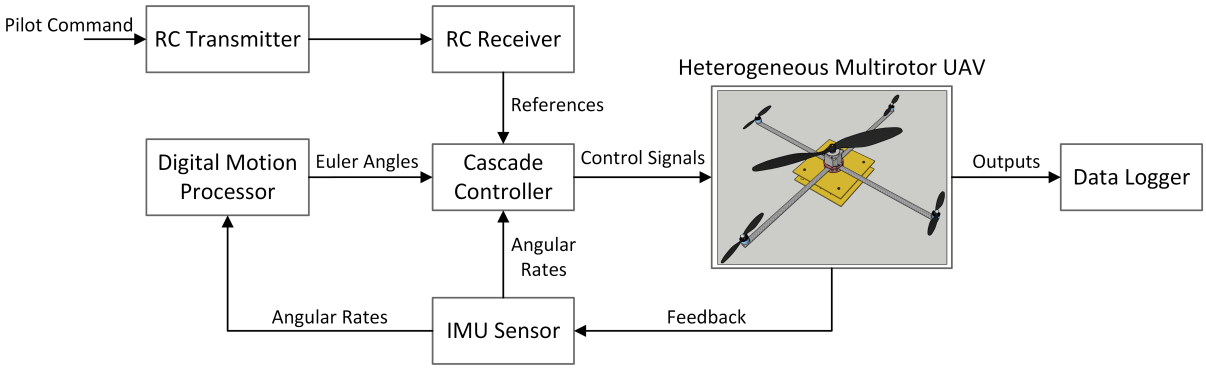

Figure 6. Flight control configuration.

Table 1. Heterogeneous multirotor UAS specifications.

Description	Details
Arm tube length	10 inches
Arm tube diameter	12 mm
Moment arm	12 inches
Main rotor propeller	2-blades (1555) 15 × 5.5 (length: 15 inches, pitch: 5.5 inches)
Boom rotor propellers	3-blades (5030) 5 × 3 (diameter: 5 inches, pitch: 3 inches)
Tilt angle of rotors	20°
Total mass	950 g

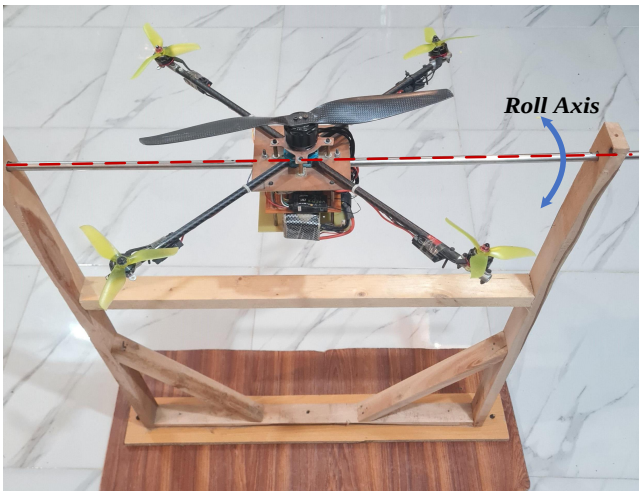

Figure 7. Test rig for roll and pitch axis.



Figure 8. Test rig for yaw axis.

Table 2. Parts used in UAS design.

Parts	Details
Micro-controller	MK64FX512VMD12
IMU	MPU6050 (build-in DMP)
Central motor	T-Motor U5 400 KV
ESC for central motor	T-Motor Air ESC 40A
Small motors	Emax RS2205 2300 KV
ESCs for small motors	Emax Lightning 30A BLHELI
Radio	Taranis x9d plus
Receiver	FrSky V8FR-II
Data logger	Teensy 3.5 SD logger

6. Experimental Analysis

For the validation of proposed strategy, system identification experiments are performed and PID controllers for inner and outer loops are designed through auto-tuning approach. Efficacy of the designed cascade PID control is evaluated through the heterogeneous multirotor's attitude response. For the cascade control structure, the inner loop is designed first and is also supposed to respond faster compared to the subsequent outer loop. Therefore, PID controller for the roll rate control is tuned first with the relay feedback experiment, followed by the roll angular control loop tuning.

6.1. Angular Rate Control Loop Tuning

6.1.1. Roll Axis

The relay feedback experiment is performed for the roll axis on the multirotor over the roll test rig. The amplitude of reference signal for the relay test is opted as 20 deg/s. Hysteresis is selected as 15 deg/s in order to prevent the gyroscopic noise. The proportional controller is chosen as $K_T = 1$. Figure 9 illustrates the response of relay feedback experiment performed on the inner loop.

A frequency sampling filter is employed to extract the information from the relay experiment data for system identification. Closed-loop frequency response for inner loop system is estimated as

$$T(e^{\frac{2\pi}{N}}) = -0.1897 - j0.6009 \tag{34}$$

Then, frequency response for the inner loop plant is estimated as

$$G(j\omega) = \frac{1}{K_T} \frac{T(e^{\frac{2\pi}{N}})}{1 - T(e^{\frac{2\pi}{N}})} = -0.3303 - j0.3382 \tag{35}$$

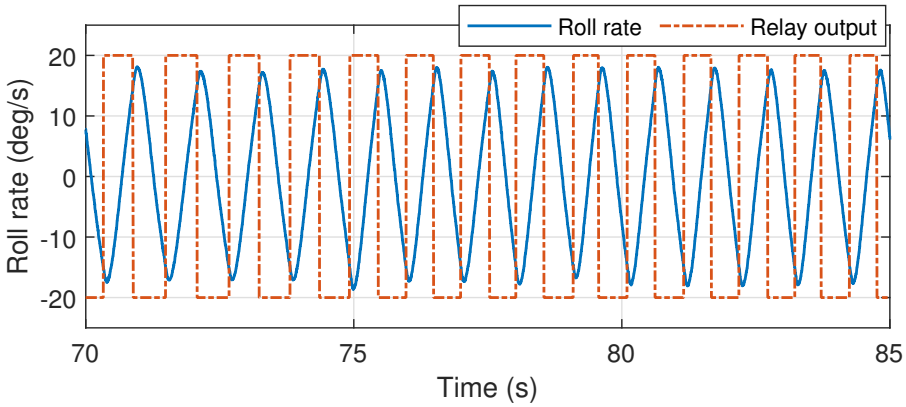

Figure 9. Inner loop relay feedback experiment for roll axis.

The fundamental frequency is also determined through FSF as $\omega_1 = 5.648$ radians. The values of K_p and d are then determined through (26) and (27), using the inner loop

frequency response in (35) and fundamental frequency value as $K_p = 2.67$ and $d = 0.136$. The integrating time delay transfer function of inner loop plant is estimated from this identified frequency response as

$$G(s) \approx \frac{K_p e^{-ds}}{s} = \frac{2.67 e^{-0.136}}{s} \tag{36}$$

Since the angular rate plant of the multirotor possesses faster dynamics, to attain the faster closed-loop response, the performance factor needs to be comparatively low. It is therefore opted as $\beta = 1$. Subsequently, the PID parameters for the roll rate control system are then obtained through (31)–(33) as $K_c = 2.422$, $\tau_I = 0.439$, and $\tau_D = 0.051$.

6.1.2. Pitch Axis

The amplitude of reference signal and the hysteresis for the relay test are selected as 30 deg/s and 20 deg/s, respectively. The proportional controller is chosen as $K_T = 1$. Figure 10 presents the response of the relay test performed on the inner loop of pitch axis. Closed-loop and inner loop plant frequency responses are estimated as

$$T(e^{\frac{2\pi}{N}}) = -0.2864 - j0.5076 \tag{37}$$

$$G(j\omega) = -0.3274 - j0.2654 \tag{38}$$

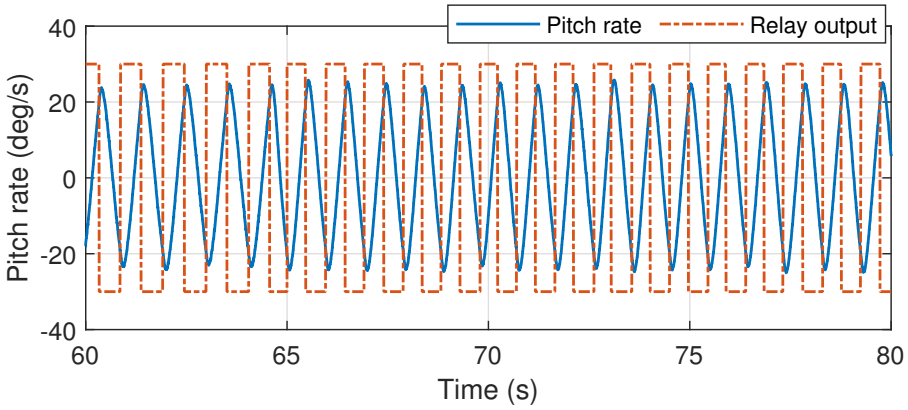

Figure 10. Inner loop relay feedback experiment for pitch axis.

The fundamental frequency is determined as $\omega_1 = 6.558$ radians. Estimated integrating delay transfer function for the pitch axis inner loop is also identified through the similar procedure:

$$G(s) = \frac{2.764\, e^{-0.135}}{s} \tag{39}$$

Moreover, the value of β for the pitch axis inner loop system is also set as 1. Subsequently, the PID parameters are then obtained as $K_c = 2.386$, $\tau_I = 0.439$, and $\tau_D = 0.048$.

6.1.3. Yaw Axis

A relay feedback experiment is also performed on yaw axis on the test rig shown in Figure 8. The reference signal and the hysteresis for the yaw relay test are selected as 25 deg/s and 10 deg/s, respectively. The proportional controller is chosen as $K_T = 1$. The response of the yaw rate for the relay feedback experiment is presented in Figure 11. Subsequently, frequency responses for the closed-loop and inner yaw loop plant are estimated as

$$T(e^{\frac{2\pi}{N}}) = -0.0561 - j0.2807 \tag{40}$$

$$G(j\omega) = -0.1156 - j0.2350 \tag{41}$$

The fundamental frequency for yaw inner loop is determined as $\omega_1 = 3.692$ radians. Estimated integrating time delay transfer function for yaw axis inner loop is identified as

$$G(s) = \frac{0.967e^{-0.123}}{s} \tag{42}$$

Performance factor, β, is also opted as 1 for tuning for inner loop controller for the yaw axis. Hence, the PID parameters for yaw rate control system are then obtained as $K_c = 7.393$, $\tau_I = 0.397$, and $\tau_D = 0.043$.

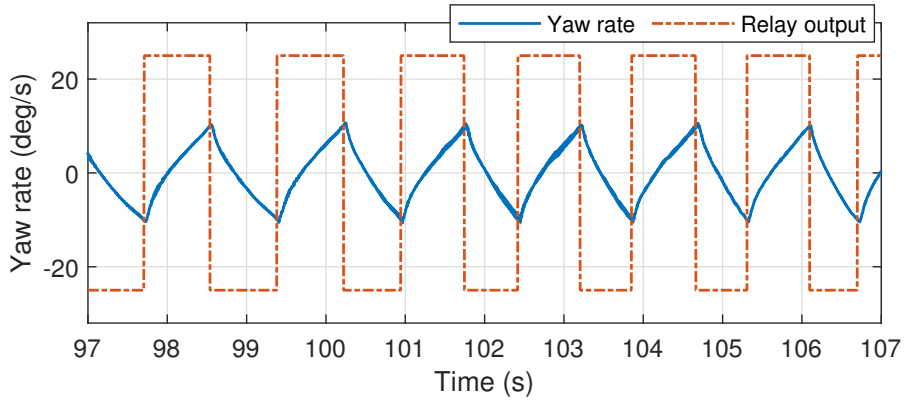

Figure 11. Inner loop relay feedback experiment for yaw axis.

6.2. Angular Loop Control Tuning

Once the PID controllers for inner loop are auto-tuned, the controller parameters for outer loop are determined using the procedure shown in Figure 12. The outer loop plant is known, which consists of an integrator (i.e., to provide roll angle through roll angular rate as in the given figure) and inner loop system which is already approximated. The estimated model representing the outer loop plant is acquired through the following integrating time delay system [42]:

$$G(s) \approx \frac{K_p e^{-(\tau_{cl}+d)s}}{s} \tag{43}$$

where τ_{cl} represents the closed-loop time constant, and time delay from the inner loop is presented as d. The integrator in this expression is from the outer loop plant, whereas the time delay is from practical estimation of the inner closed-loop system. For a controlled inner closed-loop, the gain K_p is kept as 1.

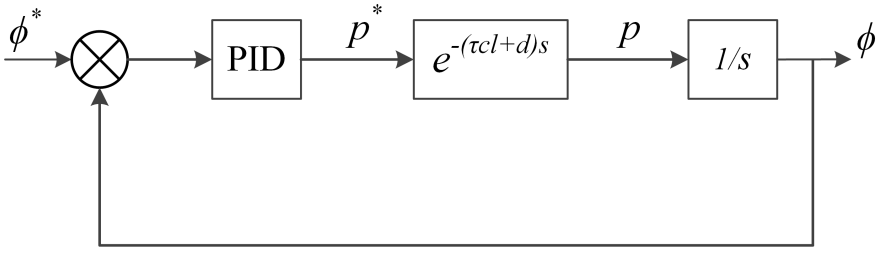

Figure 12. Roll attitude control system of the multirotor having estimated inner loop dynamics.

Since, for the stable and robust cascade control system, the response time for the outer loop needs to be slower compared to the subsequent inner loop [42], the time constant for the outer loop is selected as the double of time delay and the value of β is chosen as 2. Accordingly, parameters for the PID outer loop controller are tuned as $K_p = 1.488$, $\tau_I = 2.134$, and $\tau_D = 0.107$ for the roll axis. In a similar manner, the PID parameters for the pitch axis are determined as $K_p = 1.501$, $\tau_I = 2.115$, and $\tau_D = 0.106$. Subsequently, for the yaw axis, PID controller parameters for outer loop are tuned as $K_p = 1.644$, $\tau_I = 1.931$, and $\tau_D = 0.097$.

6.3. Flight Test Results

The designed cascade control structure, using the auto-tuned PID parameters, is implemented over the heterogeneous multirotor prototype through custom flight controller to experimentally validate the proposed idea. The sampling time of the control system is set as 4 milliseconds. The desired reference signals are received from the pilot through the RC transmitter and receiver. The tracking performance of the roll axis control system is illustrated in Figure 13, where the reference roll is being efficiently followed by the measured roll angle without steady-state error, whereas the stable angular rate response to attain the desired angular position can be analysed in Figure 14. The control signal illustrated in Figure 15 demonstrates the effort of the controller to attain the desired attitude performance. The control signal from the outer loop serves as the reference for the subsequent inner loop, as shown in Figure 3. Hence, the reference signal for roll angular rate in Figure 14 is the outer loop control system response, whereas the inner loop control signal shown in Figure 15 serves as the final control action which accordingly actuates the actuators of the multirotor. The performance of the implemented control system for pitch and yaw axis is also presented in Figures 16–20. Moreover, an anti-windup mechanism is also implemented in order to constrain the control signal within the operational range of the actuators. Anti-windup limits for the final control signal of roll and pitch control system are set as ± 20 and ± 40 for the yaw control, which can be observed in Figures 15, 18 and 20.

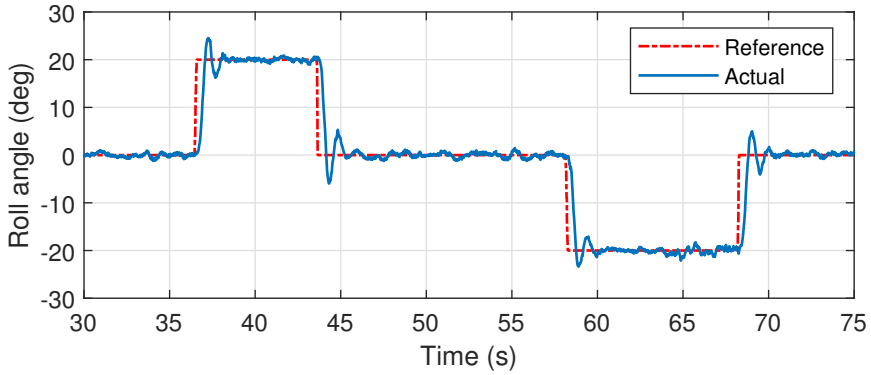

Figure 13. Roll angular response.

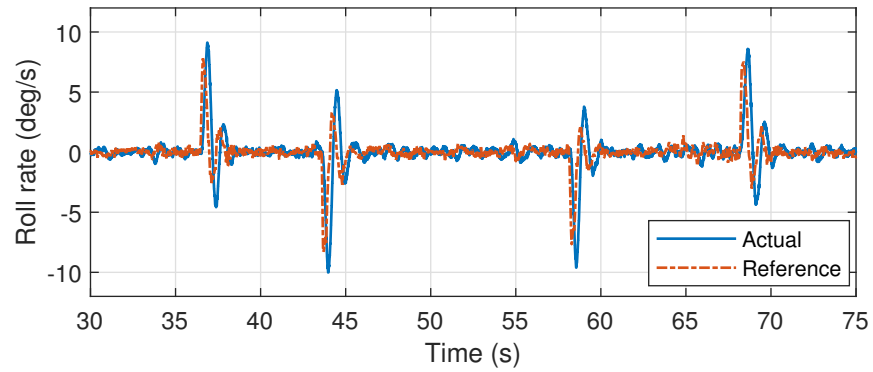

Figure 14. Roll angular rate response.

It can clearly be analysed through the presented results that the proposed cascaded PID control approach tuned through automatic tuning approach effectively provides the desired attitude response by maintaining a better time response (transient and steady-state response), containing minimum overshoots and having an improved rise and settling time.

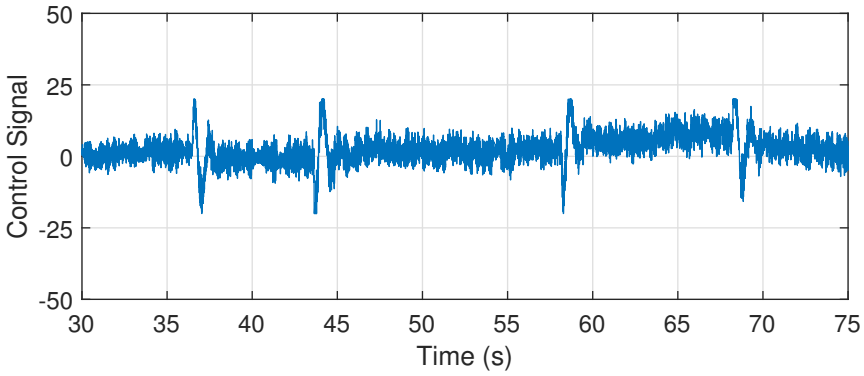

Figure 15. Control signal for roll axis tracking.

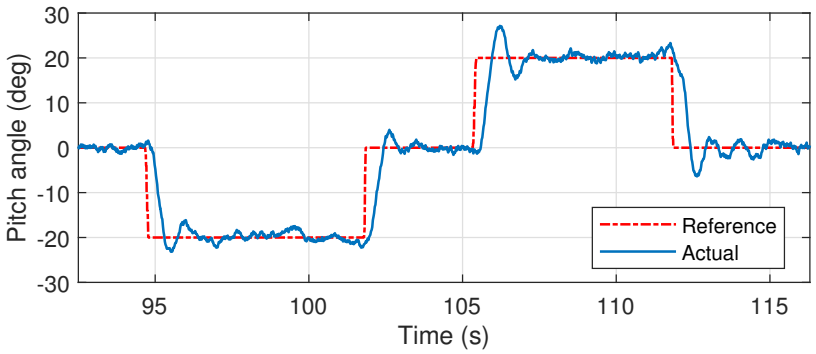

Figure 16. Pitch angular response.

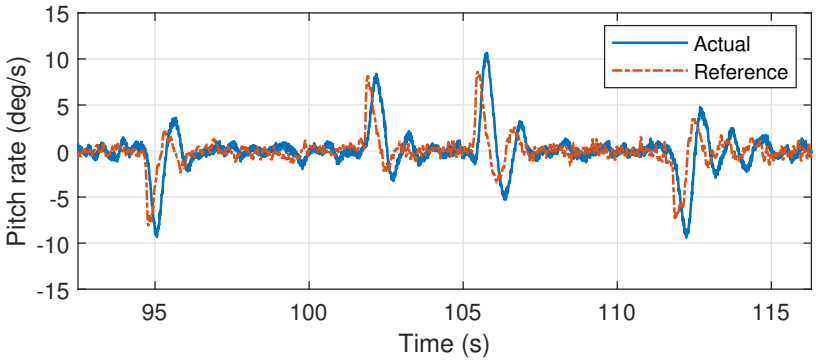

Figure 17. Pitch angular rate response.

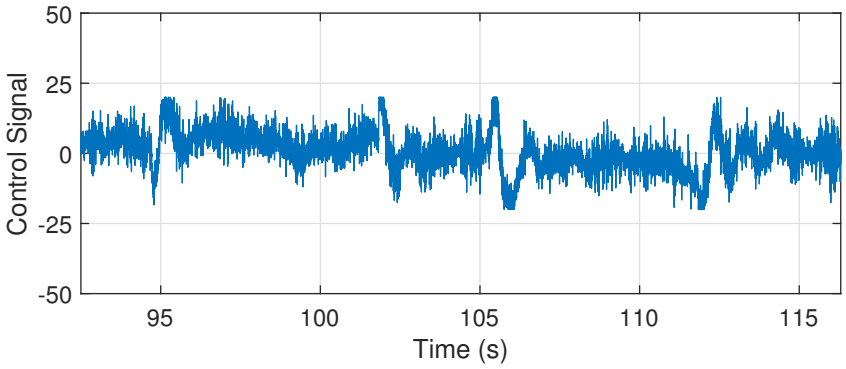

Figure 18. Control signal for pitch axis tracking.

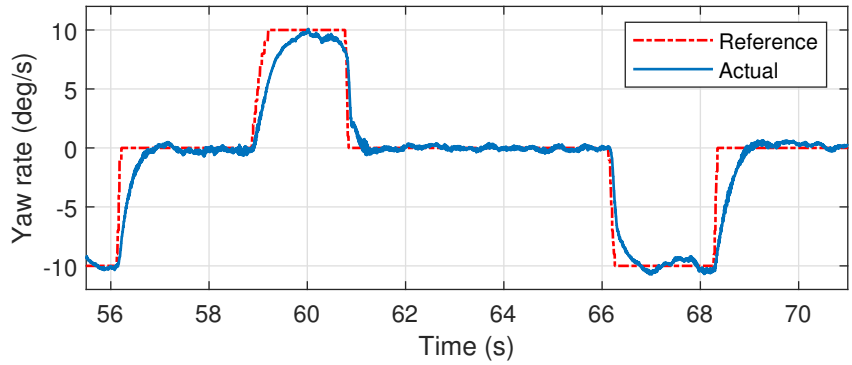

Figure 19. Yaw angular rate response.

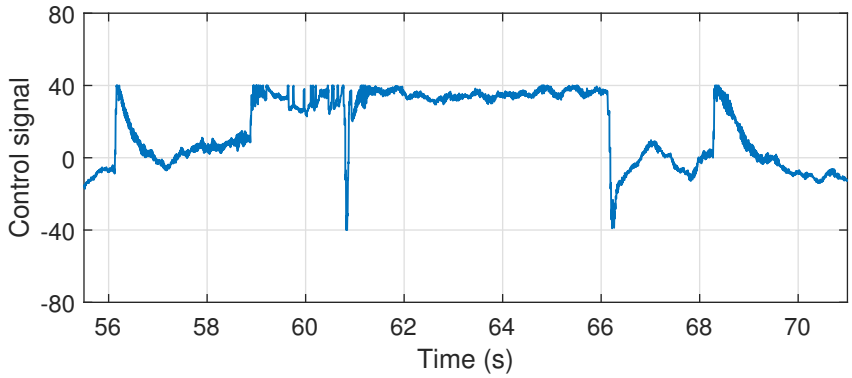

Figure 20. Control signal for yaw axis tracking.

6.4. Disturbance Rejection Analysis

The wind disturbances can be realised using an industrial fan in a controlled environment [56]. To analyse the stability and disturbance rejection capability of the designed control system, the heterogeneous multirotor is operated under the wind disturbances generated through an industrial fan, which provides the air delivery of 140 m^3/min. It can be observed from the presented experimental results in Figures 21–28 that the proposed control system is able to effectively tackle the wind disturbances. The efforts of the control system to keep the attitude response within the desired reference values, mitigating the disturbances, can also be analysed through Figures 23, 26 and 28.

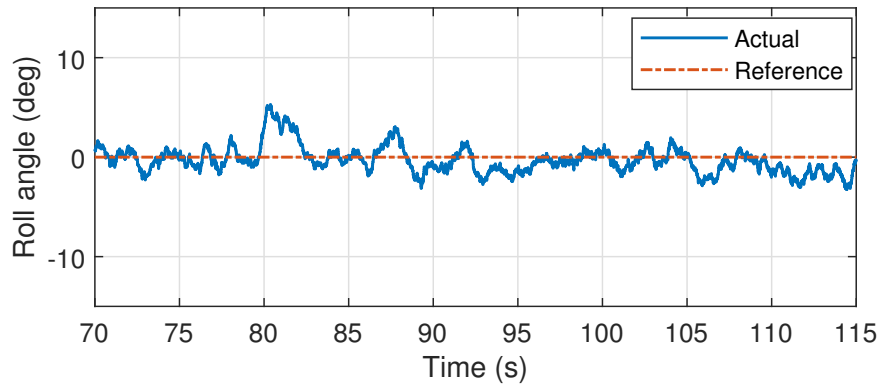

Figure 21. Roll angle.

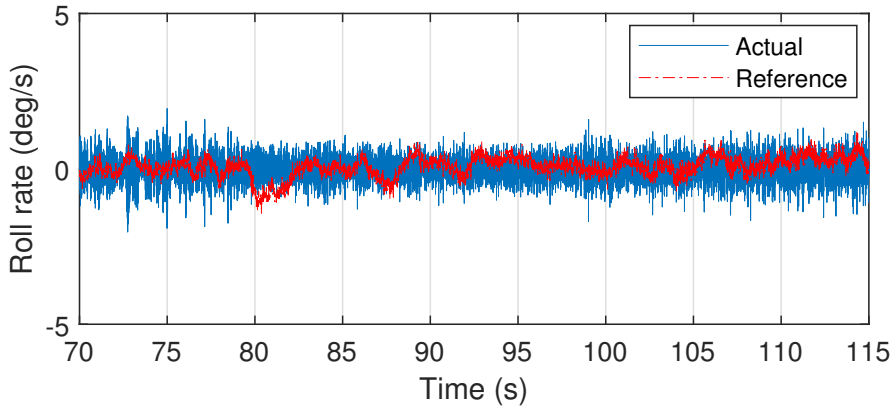

Figure 22. Roll angular angle.

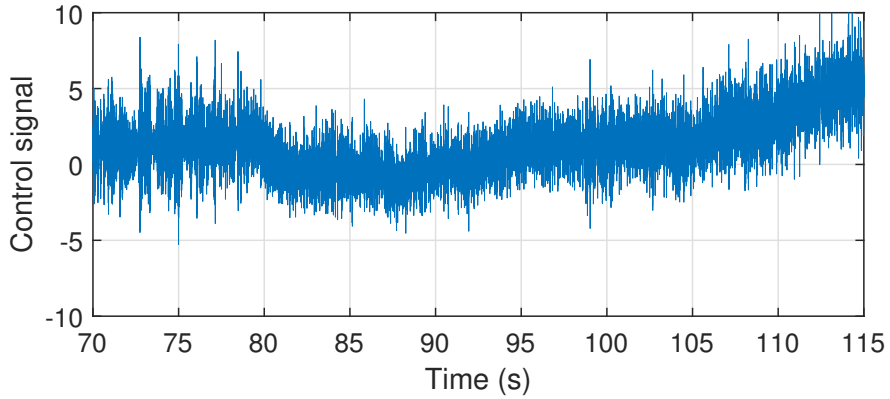

Figure 23. Control signal for roll axis.

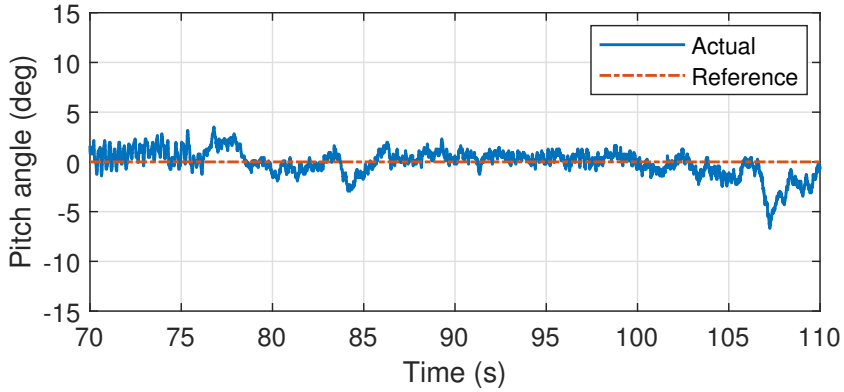

Figure 24. Pitch angle.

6.5. Comparison with Model-Based Controller Design

In order to evaluate the superiority of the proposed auto-tuning-based controller approach over the model-based controller design, the model-based PID controller is experimentally implemented over this heterogeneous multirotor through the custom flight controller. The model-based controller parameters are obtained in [26] through the multirotor dynamic model presented in Equations (5)–(9). The obtained results are compared with the auto-tuned control system responses and are presented in Figure 29.

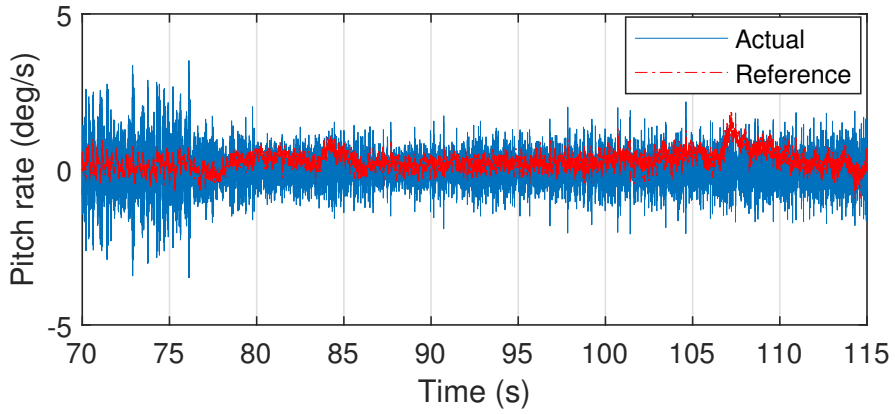

Figure 25. Pitch angular rate.

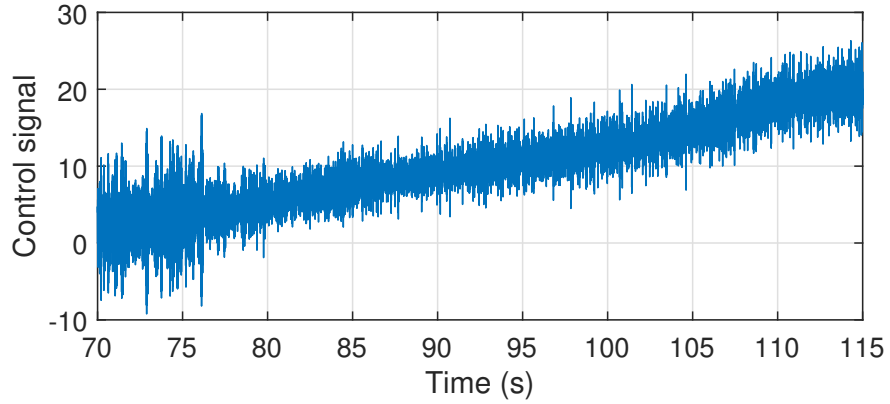

Figure 26. Control signal for pitch axis.

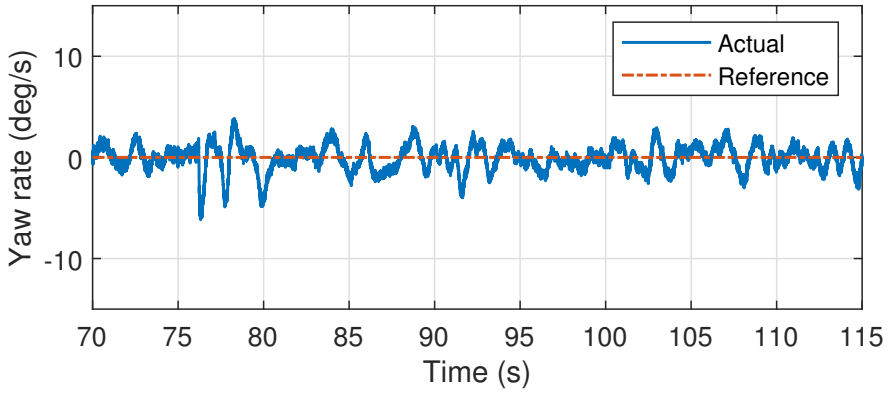

Figure 27. Yaw rate.

It can be observed that the control performance of the model-based controller design approach is not efficient when implemented experimentally over the heterogeneous multirotor prototype, whereas the proposed auto-tuning-based control system effectively provides improved performance as it contains minimal overshoots, faster transient response, and settling time, as well as improved steady state characteristics. This is due to the fact that, in the automatic tuning approach, PID controllers are designed through the experimentally acquired estimated model using relay feedback experiments and system identification, which incorporates all the actual dynamics of the complex heterogeneous multirotor configuration in the estimated models, including sensors and actuators dynamics.

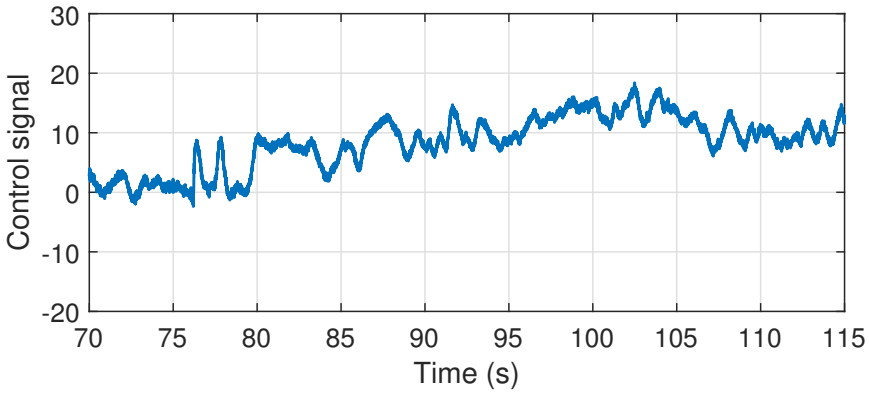

Figure 28. Control signal for yaw axis.

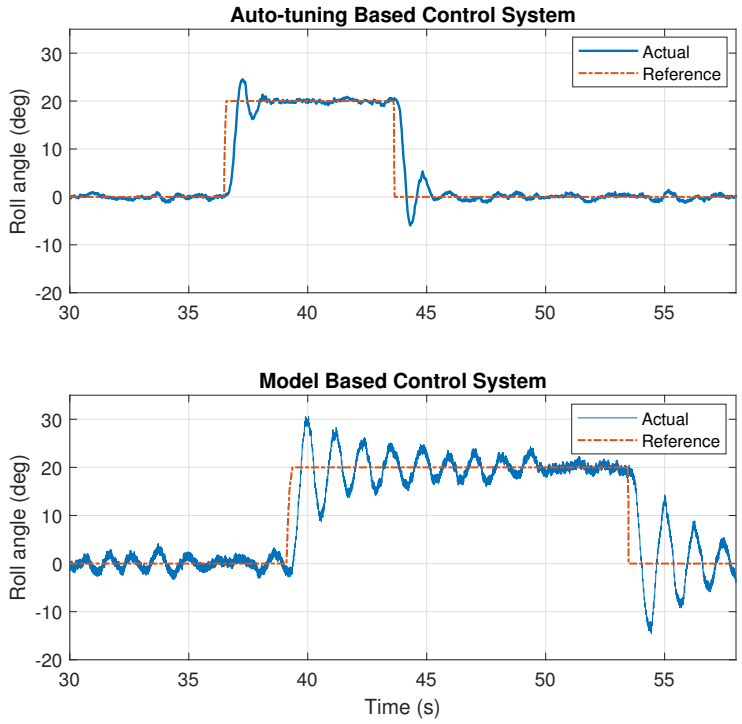

Figure 29. Control performance comparison.

The improved stability and enhanced disturbance rejection capability featured by the proposed idea is twofold:

1. A fast and robust auto-tuned cascade control system is experimentally implemented through a custom-designed flight controller over a heterogeneous multirotor.
2. Smaller arm rotors used for the control have the capability to react faster because of the decreased inertia. Consequently, the presented heterogeneous configuration with a stable control system offers substantially faster control input responses compared to a conventional multirotor.

7. Conclusions

A heterogeneous configuration of the multirotor unmanned aerial system is presented in this paper, featuring the characteristics of both multirotor and helicopter in a single rotorcraft. The major aim of the presented multirotor configuration is to achieve the comparative energy efficiency of a standard helicopter while ensuring the manoeuvrability and mechanical simplicity of a conventional multirotor. To design the stable control system for such unconventional multirotor systems in order to achieve a robust flight performance

has remained the major challenge. We have provided a stable control system for this heterogeneous multirotor through the cascaded PID control approach. PID controllers for each stage of the cascade structure are designed through an automatic tuning procedure. the custom flight controller is designed to experimentally implement the proposed cascaded control algorithm through a high-speed processor. The designed control system is experimentally validated over a heterogeneous multirotor prototype. The presented results demonstrate that the proposed idea provides a stable and robust attitude control with improved transient, as well as steady-state, response.

Author Contributions: Conceptualization, A.A.H., L.W. and A.F.; methodology, A.A.H. and L.W.; software, A.A.H. and A.S.; validation, A.A.H.; formal analysis, A.A.H.; investigation, A.A.H.; writing, A.A.H.; review and editing, A.S., L.W. and A.F.; visualization, A.A.H.; supervision, L.W. and A.F. All authors have read and agreed to the published version of the manuscript.

Funding: This research is jointly funded by RMIT University, Australia and HEC, Pakistan.

Institutional Review Board Statement: Not applicable.

Informed Consent Statement: Not applicable.

Data Availability Statement: Not applicable.

Acknowledgments: Authors acknowledge the gratitude to Manzoor Hyder alias Bilal for his technical assistance with the project and Shahzeb Ansari for his helpful suggestions during the write-up and modification of this paper.

Conflicts of Interest: The authors declare no conflict of interest.

References

1. Hu, D.; Pei, Z.; Tang, Z. Single-Parameter-Tuned Attitude Control for Quadrotor with Unknown Disturbance. *Appl. Sci.* **2020**, *10*, 5564. [CrossRef]
2. Floreano, D.; Wood, R.J. Science, technology and the future of small autonomous drones. *Nature* **2015**, *521*, 460–466. [CrossRef] [PubMed]
3. Hua, H.; Fang, Y.; Zhang, X.; Lu, B. A Novel Robust Observer-Based Nonlinear Trajectory Tracking Control Strategy for Quadrotors. *IEEE Trans. Control Syst. Technol.* **2020** , *29*, 1952–1963. [CrossRef]
4. Zheng, D.; Wang, H.; Wang, J.; Chen, S.; Chen, W.; Liang, X. Image-based visual servoing of a quadrotor using virtual camera approach. *IEEE/ASME Trans. Mechatron.* **2016**, *22*, 972–982. [CrossRef]
5. Mahony, R.; Kumar, V.; Corke, P. Multirotor aerial vehicles: Modeling, estimation, and control of quadrotor. *IEEE Robot. Autom. Mag.* **2012**, *19*, 20–32. [CrossRef]
6. Jee, S.H.; Cho, H.C.; Kim, J. The Experimental Modeling of Quad-Rotor Actuators with Undefined Hardware Errors for Safety-Flight. *Electronics* **2020**, *9*, 579. [CrossRef]
7. He, X.; Kou, G.; Calaf, M.; Leang, K.K. In-Ground-Effect Modeling and Nonlinear-Disturbance Observer for Multirotor Unmanned Aerial Vehicle Control. *J. Dyn. Syst. Meas. Control* **2019**, *141*. [CrossRef]
8. Liu, H.; Xi, J.; Zhong, Y. Robust attitude stabilization for nonlinear quadrotor systems with uncertainties and delays. *IEEE Trans. Ind. Electron.* **2017**, *64*, 5585–5594. [CrossRef]
9. Song, S.H.; Yeon, G.Y.; Shon, H.W.; Choi, H.R. Design and Control of Soft Unmanned Aerial Vehicle 'S-CLOUD'. *IEEE/ASME Trans. Mechatron.* **2020**, *26*, 267–275. [CrossRef]
10. Chen, Z.; Stol, K.; Richards, P. Preliminary design of multirotor UAVs with tilted-rotors for improved disturbance rejection capability. *Aerosp. Sci. Technol.* **2019**, *92*, 635–643. [CrossRef]
11. UNICEF-Supply-Division. How Drones Can Be Used to Combat COVID-19. Rapid Guidance, UNICEF. 2020. Available online: https://www.unicef.org/supply/documents/how-drones-can-be-used-combat-covid-19 (accessed on 1 February 2022).
12. Kunovjanek, M.; Wankmüller, C. Containing the COVID-19 pandemic with drones-Feasibility of a drone enabled back-up transport system. *Transp. Policy* **2021**, *106*, 141–152. [CrossRef] [PubMed]
13. González Jorge, H.; González de Santos, L.M.; Fariñas Álvarez, N.; Martínez Sánchez, J.; Navarro Medina, F. Operational Study of Drone Spraying Application for the Disinfection of Surfaces against the COVID-19 Pandemic. *Drones* **2021**, *5*, 18. [CrossRef]
14. Śledziowski, J.; Terefenko, P.; Giza, A.; Forczmański, P.; Łysko, A.; Maćków, W.; Stępień, G.; Tomczak, A.; Kurylczyk, A. Application of Unmanned Aerial Vehicles and Image Processing Techniques in Monitoring Underwater Coastal Protection Measures. *Remote Sens.* **2022**, *14*, 458. [CrossRef]
15. Di Gennaro, S.F.; Toscano, P.; Gatti, M.; Poni, S.; Berton, A.; Matese, A. Spectral Comparison of UAV-Based Hyper and Multispectral Cameras for Precision Viticulture. *Remote Sens.* **2022**, *14*, 449. [CrossRef]

16. Junaid, A.; Konoiko, A.; Zweiri, Y.; Sahinkaya, M.; Seneviratne, L. Autonomous wireless self-charging for multi-rotor unmanned aerial vehicles. *Energies* **2017**, *10*, 803. [CrossRef]
17. Kingry, N.; Towers, L.; Liu, Y.C.; Zu, Y.; Wang, Y.; Staheli, B.; Katagiri, Y.; Cook, S.; Dai, R. Design, Modeling and Control of a Solar-Powered Quadcopter. In Proceedings of the 2018 IEEE International Conference on Robotics and Automation (ICRA), Brisbane, Australia, 21–25 May 2018; pp. 1251–1258. [CrossRef]
18. Driessens, S.; Pounds, P.E. Towards a more efficient quadrotor configuration. In Proceedings of the 2013 IEEE/RSJ International Conference on Intelligent Robots and Systems, Tokyo, Japan, 3–7 November 2013; pp. 1386–1392. [CrossRef]
19. Leishman, G.J. *Principles of Helicopter Aerodynamics with CD Extra*; Cambridge University Press: Cambridge, UK, 2006.
20. Pounds, P.; Mahony, R. Small-scale aeroelastic rotor simulation, design and fabrication. In Proceedings of the Australasian Conference on Robotics and Automation, Citeseer, Sydney, Australia, 5–7 December 2005; pp. 1–8.
21. Seddon, J.M.; Newman, S. *Basic Helicopter Aerodynamics*; John Wiley and Sons: Hoboken, NJ, USA, 2011; Volume 40.
22. Yan, K.; Chen, M.; Wu, Q.; Lu, K. Robust attitude fault-tolerant control for unmanned autonomous helicopter with flapping dynamics and actuator faults. *Trans. Inst. Meas. Control* **2018**, *41*, 0142331218775477. [CrossRef]
23. Driessens, S.; Pounds, P. The triangular quadrotor: A more efficient quadrotor configuration. *IEEE Trans. Robot.* **2015**, *31*, 1517–1526. [CrossRef]
24. Qin, Y.; Xu, W.; Lee, A.; Zhang, F. Gemini: A Compact Yet Efficient Bi-Copter UAV for Indoor Applications. *IEEE Robot. Autom. Lett.* **2020**, *5*, 3213–3220. [CrossRef]
25. Emran, B.J.; Najjaran, H. A review of quadrotor: An underactuated mechanical system. *Annu. Rev. Control* **2018**, *46*, 165–180. [CrossRef]
26. Hoshu, A.A.; Wang, L.; Fisher, A.; Sattar, A. Cascade control for heterogeneous multirotor UAS. *Int. J. Intell. Unmanned Syst.* **2021**. [CrossRef]
27. Eskandarpour, A.; Sharf, I. A constrained error-based MPC for path following of quadrotor with stability analysis. *Nonlinear Dyn.* **2020**, *99*, 899–918. [CrossRef]
28. Zhou, L.; Zhang, J.; She, H.; Jin, H. Quadrotor UAV flight control via a novel saturation integral backstepping controller. *Automatika* **2019**, *60*, 193–206. [CrossRef]
29. Zhao, K.; Zhang, J.; Ma, D.; Xia, Y. Composite disturbance rejection attitude control for quadrotor with unknown disturbance. *IEEE Trans. Ind. Electron.* **2019**, *67*, 6894–6903. [CrossRef]
30. Xuan-Mung, N.; Hong, S.K. Robust backstepping trajectory tracking control of a quadrotor with input saturation via extended state observer. *Appl. Sci.* **2019**, *9*, 5184. [CrossRef]
31. Razmi, H.; Afshinfar, S. Neural network-based adaptive sliding mode control design for position and attitude control of a quadrotor UAV. *Aerosp. Sci. Technol.* **2019**, *91*, 12–27. [CrossRef]
32. Pi, C.H.; Ye, W.Y.; Cheng, S. Robust quadrotor control through reinforcement learning with disturbance compensation. *Appl. Sci.* **2021**, *11*, 3257. [CrossRef]
33. Kang, C.; Park, B.; Choi, J. Scheduling PID Attitude and Position Control Frequencies for Time-Optimal Quadrotor Waypoint Tracking under Unknown External Disturbances. *Sensors* **2022**, *22*, 150. [CrossRef]
34. Mystkowski, A. Robust control of the micro UAV dynamics with an autopilot. *J. Theor. Appl. Mech.* **2013**, *51*, 751–761.
35. Pixhawk-Ardupilot. PX4 Autopilot. Available online: https://docs.px4.io/master/en/flight_stack/controller_diagrams.html (accessed on 1 February 2022).
36. Micropilot. Micropilot Autopilots. Available online: https://www.micropilot.com/index.htm (accessed on 1 February 2022).
37. Paparrazzi. Paparazzi UAV Flight Controllers. Available online: https://wiki.paparazziuav.org (accessed on 1 February 2022).
38. Hoshu, A.A.; Fisher, A.; Wang, L. Cascaded Attitude Control For Heterogeneous Multirotor UAS For Enhanced Disturbance Rejection. In Proceedings of the 2019 Australian and New Zealand Control Conference (ANZCC), Auckland, New Zealand, 27–29 November 2019; pp. 110–115. [CrossRef]
39. Hoffer, N.V.; Coopmans, C.; Jensen, A.M.; Chen, Y. A survey and categorization of small low-cost unmanned aerial vehicle system identification. *J. Intell. Robot. Syst.* **2014**, *74*, 129–145. [CrossRef]
40. Wang, L.; Cluett, W. Tuning PID controllers for integrating processes. *IEE Proc. Control Theory Appl.* **1997**, *144*, 385–392. [CrossRef]
41. Wang, L.; Desarmo, M.L.; Cluett, W.R. Real-time estimation of process frequency response and step response from relay feedback experiments. *Automatica* **1999**, *35*, 1427–1436. [CrossRef]
42. Wang, L. *PID Control System Design and Automatic Tuning Using MATLAB/Simulink*; John Wiley and Sons: Hoboken, NJ, USA, 2020.
43. Griffiths, D.; Leishman, J. A study of dual-rotor interference and ground effects using a free-vortex wake model. In Proceedings of the 58th Annual Forum and Technology Display of the American Helicopter Assoc, Montreal, QC, Canada, 11 June 2002.
44. Maisel, M.D. *The History of the XV-15 Tilt Rotor Research Aircraft: From Concept to Flight*; National Aeronautics and Space Administration, Office of Policy and Plans, NASA History Division: Washington, DC, USA, 2000.
45. Leishman, J.G. Development of the autogiro: A technical perspective. *J. Aircr.* **2004**, *41*, 765–781. [CrossRef]
46. APC-Prop. APC Propeller Performance Data. 2021. Available online: https://www.apcprop.com/technical-information/performance-data (accessed on 1 February 2022).
47. Deters, R.W.; Ananda Krishnan, G.K.; Selig, M.S. Reynolds number effects on the performance of small-scale propellers. In Proceedings of the 32nd AIAA Applied Aerodynamics Conference, Atlanta, GA, USA, 16–20 June 2014; p. 2151.
48. T-Motor. U5 KV400 Testing Data. Available online: https://store.tmotor.com/goods.php?id=318 (accessed on 1 February 2022).

49. T-Motor. AS2814 KV1050 Test Report. Available online: https://store.tmotor.com/goods.php?id=939 (accessed on 1 February 2022).
50. Bouabdallah, S.; Murrieri, P.; Siegwart, R. Design and control of an indoor micro quadrotor. In Proceedings of the IEEE International Conference on Robotics and Automation, Proceedings, ICRA'04, New Orleans, LA, USA, 26 April–1 May 2004; Volume 5; pp. 4393–4398. [CrossRef]
51. Wang, L. Automatic tuning of PID controllers using frequency sampling filters. *IET Control Theory Appl.* **2017**, *11*, 985–995. [CrossRef]
52. Sattar, A.; Wang, L.; Mohamed, A.; Panta, A.; Fisher, A. System Identification of Fixed-wing UAV with Multi-segment Control Surfaces. In Proceedings of the 2019 Australian and New Zealand Control Conference (ANZCC), Auckland, New Zealand, 27–29 November 2019; pp. 76–81. [CrossRef]
53. Kreyszig, E. *Advanced Engineering Mathematics*; John Wiley and Sons: Hoboken, NJ, USA, 2010.
54. Wang, L. *From Plant Data to Process Control: Ideas for Process Identification and PID Design*; CRC Press: Boca Raton, FL, USA, 2000.
55. InvenSense. Embedded Motion Driver v5.1.1 Apis Specification. Doc: SW-EMD-REL-5.1.1, Doc Rev:1.0 . 2012. Available online: https://www.digikey.com/Site/Global/Layouts/DownloadPdf.ashx?pdfUrl=4012F20DDE8F4095B10E31923C2F7EF2 (accessed 1 February 2022).
56. Gu, X.; Xian, B.; Li, J. Model free adaptive control design for a tilt trirotor unmanned aerial vehicle with quaternion feedback: Theory and implementation. *Int. J. Adapt. Control Signal Process.* **2022**, *36*, 122–137. [CrossRef]